

6

c0006 Floating Zone Growth of Silicon

Andris Muiznieks^{1,†}, Janis Virbulis¹, Anke Lüdge²,
Helge Riemann², Nico Werner²

¹DEPARTMENT OF PHYSICS, UNIVERSITY OF LATVIA, RIGA, LATVIA;
²INSTITUTE OF CRYSTAL GROWTH, BERLIN, GERMANY

[AU1]

CHAPTER OUTLINE

6.1 Basics of the Floating Zone Silicon Crystal Growth	2
6.1.1 History: From Zone Melting Purification to the Crucible-free Silicon Crystal Growth.....	2
6.1.2 Fundamentals of the FZ Technology	4
6.1.2.1 FZ Setup	4
6.1.2.2 Main Steps of the FZ Process.....	5
6.1.3 Crucial FZ Details.....	8
6.1.3.1 Origin and Analysis of Failures.....	8
6.1.3.2 Rotation and Pull Rates	9
6.1.3.3 Stability of the Molten Zone and Growth Angle.....	10
6.1.3.4 The Feed Rod	11
6.1.3.5 Induction Coil and Arcing.....	11
6.1.4 FZ Crystal Morphology: Ridges and Orientation	12
6.1.4.1 Growth Habitus	12
6.1.5 Doping Techniques and Impurity Distribution.....	13
6.1.6 Recent Development	13
6.2 Automation of the Floating Zone Process Using Model-Based Control	15
6.2.1 Motivation	15
6.2.2 Description of the Measurement System	15
6.2.3 Modeling of the Floating Zone Process.....	16
6.2.4 Choice of Reference and Manipulated Variables	18
6.2.4.1 Creating the Thin Neck.....	18
6.2.4.2 Growing the Crystal Cone	18
6.2.4.3 Growing the Cylinder	18
6.2.5 Regulated Growth of the Avogadro Crystal	18

2 HANDBOOK OF CRYSTAL GROWTH

6.3 Mathematical Modeling of the Floating Zone Silicon Growth.....	19
6.3.1 Introduction.....	19
6.3.2 Historical Overview.....	21
6.3.3 Mathematical Models.....	22
6.3.3.1 Electromagnetic Field.....	23
6.3.3.2 Temperature Field.....	23
6.3.3.3 Melt Flow.....	24
6.3.3.4 Impurity Distribution.....	25
6.3.3.5 Shape of Interfaces.....	25
6.3.3.6 Thermomechanical Stress.....	26
6.3.3.7 Transient Modeling.....	26
6.3.4 Exemplary Results.....	27
6.3.4.1 Electromagnetic Field.....	27
6.3.4.2 Temperature Field.....	28
6.3.4.3 Melt Flow and Impurity Distribution.....	29
6.3.4.4 Shape of Interfaces.....	32
6.3.4.5 Stress.....	34
6.3.4.6 Transient Modeling.....	34
6.3.5 Summary, Conclusions, and Outlook.....	36
References.....	36

s0010 6.1 Basics of the Floating Zone Silicon Crystal Growth

s0015 6.1.1 History: From Zone Melting Purification to the Crucible-free Silicon Crystal Growth

p0010 Zone melting is a technique that was mainly applied for purifying congruently melting substances in a physical way. Originally, a narrow heater generates a molten zone in the solid substance being in a horizontal boat-like crucible made of a material that must not pollute that substance. If the molten zone is continuously shifted through the material in the boat by the relative movement between boat and heater, impurities are partly gathered in the molten zone due to their almost increased solubility in the liquid state according to the segregation coefficient k :

$$k = c_s/c_l \quad (6.1)$$

where c_s and c_l are the solubilities in the solid and in the liquid state, respectively.

p0015 In that way, impurities are traveling with the molten zone to one end of the rod where they are deposited in the last solidifying material. As a result, most material of the rod becomes purer at the cost of the end part. Multiple zone melting enables high purity grades as needed for semiconductors. Unfortunately, horizontal zone melting fails for

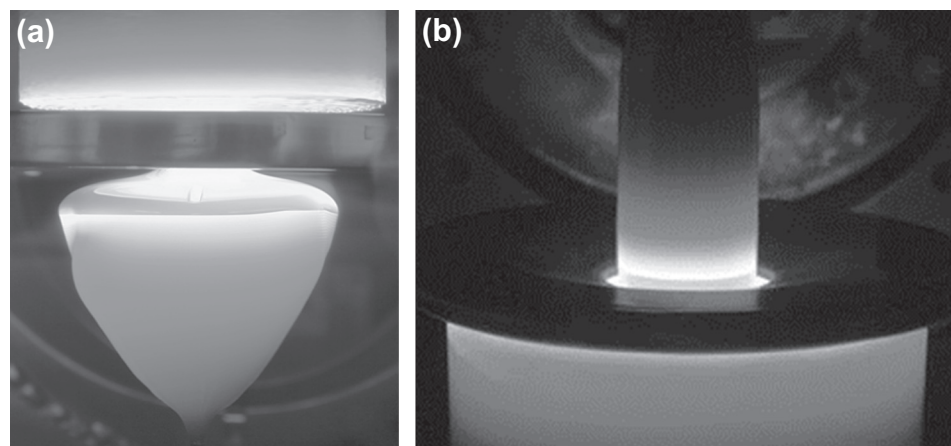
silicon, the most important semiconductor, because any material for the boat including quartz markedly reacts with the silicon melt, and silicon adheres mostly at the boat causing cracks during cooling down due to different thermal contraction.

p0020 However, amazingly large and rather pure silicon single crystals can be grown directly from the melt in a quartz crucible bowl after the well-established Czochralski (CZ) method, but CZ silicon does not fit all needs for some important electronic devices because the eroding crucible introduces oxygen into the silicon forming SiO_x precipitates and thermal donors. Other specific impurities are carbon and B, Al, Fe, etc., which limit resistivity and carrier lifetime of the material.

p0025 In order to overcome these drawbacks, the crucible-free FZ method was invented in the early 1950s [1,2], as a contactless vertical zone melting technique. Starting with a seed crystal, the FZ process becomes a crucible-free crystal growth method, which is widely technically used [3]. Silicon suits this method very well, because the “floating” molten zone is neatly stabilized by the strong surface tension and is located between the vertically positioned growing crystal at the bottom and the melting silicon feed rod at the top. It is commonly generated by the contactless inductive heating via the RF (c. 3 MHz) magnetic field of a one-turn induction coil. The zone “floats” upward due to the relative movement between the heating coil and the silicon rods. The induction coil and the RF generator are fixed and crystal and rod are moved downward while rotating.

p0030 Radiative heating, instead of inductive, was also investigated, especially in space experiments, but it is only feasible if the crystal diameter is below c. 30 mm [4].

p0035 The FZ process also works if the feed rod is placed on the bottom as a pedestal and the crystal is pulled upward. This pedestal growth method is inherently more stable, but the diameter of the crystal is markedly smaller than that of the feed rod and of the inductor hole as shown in Figure 6.1(b). This method also has industrial relevance as a technique for producing the slim rods needed as filaments for the Siemens process.



f0010

FIGURE 6.1 Floating zone (a) and pedestal (b) crystal growth [4].

4 HANDBOOK OF CRYSTAL GROWTH

p0040 Both, FZ and CZ silicon crystals can be grown in a dislocation-free structure after eliminating all dislocations by the thin-neck method after Dash [5]. The dislocation-free growth is absolutely necessary for single crystals with a diameter of more than c. 40 mm in order to avoid the rapidly increasing multiplication of any new dislocations due to the higher thermal stress, resulting very quickly in polycrystallinity. The diameter of FZ silicon is currently limited to 200 mm (Figure 6.2), mainly by high voltage breakthroughs at the “pancake inductor” [6]. In contrast to this, CZ silicon crystals can be grown with greater diameter of up to 400 mm.

p0045 FZ and CZ silicon complement each other. Compared with CZ silicon, typical impurity concentrations of FZ silicon are two to three orders of magnitude smaller and electric resistivities of up to 30 kOhm cm and carrier lifetimes τ of about 8000 μ s are achievable. Especially the very low oxygen concentration prevents any oxide precipitation in thermal processing, which is important for high voltage applications. The worldwide production of FZ silicon continuously rises, but not as fast as that for CZ, so, the percentage of the FZ silicon production has dropped from 20% in the 1980s to about 5% nowadays.

p0050 However, FZ silicon is essential and indispensable for high power electronics as well as for innovative devices. The main objectives of the present research on FZ silicon are innovative concepts for crystal diameters beyond 200 mm, FZ crystal growth directly from much cheaper Si feedstock, e.g., fluid bed granulate and a cost reduction of FZ silicon for PV application.

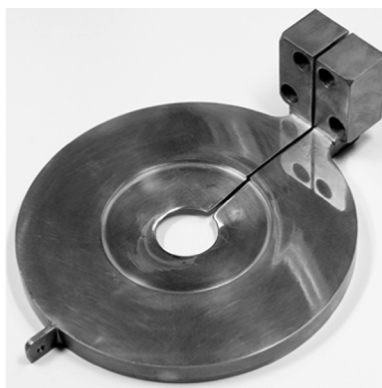
s0020 6.1.2 Fundamentals of the FZ Technology

s0025 6.1.2.1 FZ Setup

p0055 The essential components of an FZ crystal puller are the vacuum-tight growth chamber containing the protection gas atmosphere, and the upper pulling shaft and the lower one, which can independently vertically translate and rotate. The former carries the feed

f0015 **FIGURE 6.2** A silicon monocrystal with 200-mm diameter grown at Siltronic AG using the floating zone process. Photo: Siltronic AG.





f0020

FIGURE 6.3 Induction coil suitable for growing floating zone crystals.

rod mount and the latter the seed mount. The heart of the puller is the induction coil (Figure 6.3), which is connected to the coaxial RF power feedthrough as well as to the cooling water supply. State of the art is a flat, one-turn pancake induction coil, which has to enclose the molten zone but avoid any contact with it. Several geometric items of the inductor, like slots, diameters, and angles, define shape and structure of the RF magnetic field and, finally, the distribution of the induced thermal power and the electrodynamic forces on the melt surface. The induction coil significantly determines yield and success of the FZ crystal growth.

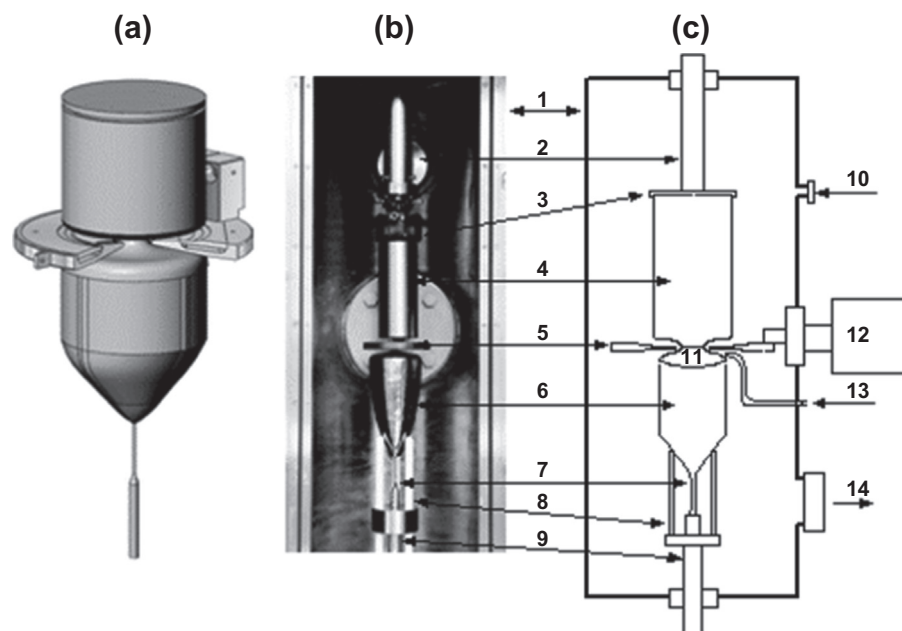
p0060 Auxiliary installations in the setup are heat reflection shields, a feed rod preheating system, a mechanical supporting system for big crystals, and the supplies for vacuum and protecting gas with controlled gas composition, a dosing apparatus for the doping gas and measuring devices for diameters, and zone height required for automatic process control.

s0030 6.1.2.2 Main Steps of the FZ Process

p0065 After assembling the shaped and cleaned silicon feed rod and the oriented seed crystal of pencil shape in their mounts, Figure 6.4(b) and (c) 4 and 7, the growth chamber will be closed, evacuated, and commonly filled with high purity argon as protecting gas. Preheating the conical lower end of the feed rod to above 450 °C raises the intrinsic electric conductivity so that the RF field of the coil can inductively heat up the cone tip above the melting point (1413 °C), generating a big hanging melt drop held by adhesion and surface tension.

p0070 The seed crystal is moved upward until it is close below the drop where it heats up for some time for reducing the temperature difference in relation to the melt. Then it is further moved up until it dips into the melt drop from the bottom, whereby the seed melts back a bit and the seed-melt interface smoothes. The oriented crystallization is initiated by lowering the RF power and pulling down the seed with a rate of 6–12 mm/min. Doing this, the drop is shrunk and stretched and the monocrystalline thin neck of

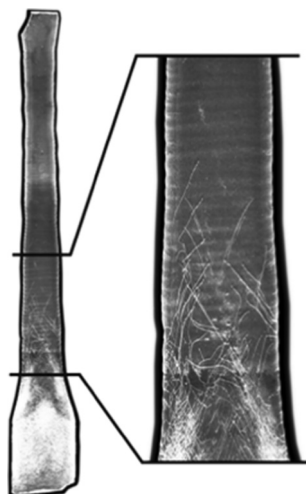
6 HANDBOOK OF CRYSTAL GROWTH



f0025 **FIGURE 6.4** Setup of a floating zone puller [4] (a) three-dimensional scheme, (b) model setup of the chamber, (c) cross-section through a growth chamber. 1, growth chamber; 2, upper spindle; 3, rod holder; 4, feed rod; 5, induction coil; 6, growing crystal; 7, seed with thin neck; 8, crystal support; 9, lower spindle; 10, gas inlet; 11, molten zone; 12, RF generator; 13, doping gas supply; 14, pump.

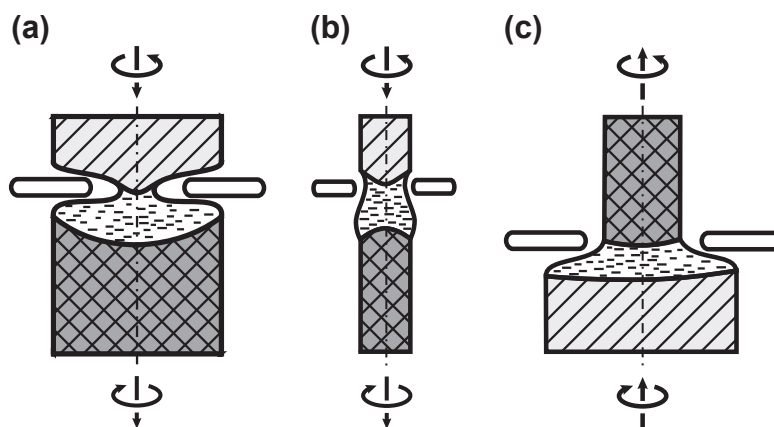
2–3 mm thickness grows initially with the high dislocation density of the seed generated by the thermal shock from before. In this phase, a tiny flat melt zone is establishing, and the so-called thin neck can grow under very low thermomechanical stress unable to initiate further dislocation gliding and multiplication. Because, practically, all dislocation lines deviate from the growth axis, they leave the thin neck, which becomes dislocation-free after a few centimeters of growth length. This technique, as shown in Figure 6.5, was originally invented by Dash for CZ silicon growth [5] and works pretty certainly for several crystal orientations but generally not for the $\langle 110 \rangle$ direction because it is the preferred orientation of dislocation lines in silicon.

p0075 If the crystal neck is dislocation-free and the growth is not seriously disturbed, the crystal will stay in that state even if the diameter increases because of the very high generation energy of dislocations in contrast to that of dislocation multiplication. Therefore, both the inductor current and the speed of the upper feed rod can be gradually increased in order to raise the melt flow and to increase the molten zone, resulting in a steadily rising diameter of the crystal obtaining a conical shape, see Figure 6.1(a). This has to be done smoothly and steadily especially regarding the shape of the free melt meniscus at the crystallization interface because of the danger of spilling out of the melt or of a thermally induced loss of the dislocation-free structure.



f0030 **FIGURE 6.5** X-ray topogram of a $\langle 111 \rangle$ thin neck (5 mm \times 40 mm) with vanishing dislocations, enlargement on the right: no further dislocations after about 20 mm [4].

p0080 A distinctive feature of the FZ method was invented with the needle-eye technique (Figure 6.6), which allows overcoming the dilemma of the limited capillary stability of a molten zone that becomes unstable if its height exceeds a critical value of c. 17 mm for silicon [4]. Using the needle-eye technique, the molten zone forms a narrow neck of c. 20 mm diameter, which is fed through and enclosed by the inner hole of the inducing coil as shown in Figure 6.6(a) in comparison to the non-needle eye technique (b) with which only small diameters can be reached.



f0035 **FIGURE 6.6** Floating zone needle-eye technique (a), non-needle-eye crystal growth for small diameters (b) and pedestal crystal growth (c) [4].

8 HANDBOOK OF CRYSTAL GROWTH

p0085 In that way, the height of the zone can be held below the critical value because the relevant diameter of the neck of the zone can stay small and almost independent on the crystal diameter. Moreover, the crystal diameter can exceed the diameter of the feed rod in contrast to the pedestal technique, where the diameters of pedestal or inductor hole, whichever is greater, cannot be exceeded.

p0090 If the growing FZ crystal is approaching the target diameter, the transient growth process has to be changed to an almost stationary one with constant diameter and pulling rate. The gain of the induced power has to be carefully stopped and the feed rate has to be balanced regarding the target diameter. This is accompanied with distinct changes of the melt meniscus shape and the thermal stress field and is the most critical phase of the FZ process.

p0095 The subsequent growth of the cylindrical part is almost stationary. Only the changing lengths of crystal and feed rod require slight corrections of the RF power during the whole process.

p0100 If the desired crystal length is grown or the feed is coming to its end, the process will be finished by lowering the inductor power and subsequently stopping the feed rod. The shrinking molten zone finally divides due to the move of the crystal carrying the remaining melt, which is gradually solidifying.

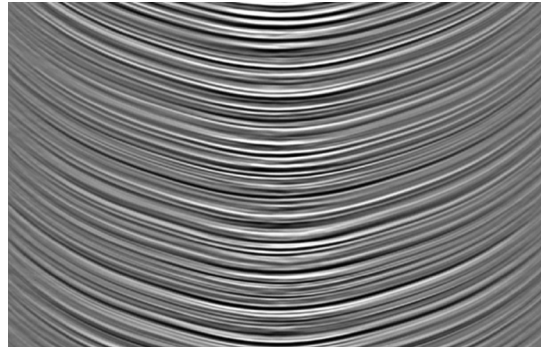
p0105 At the end of the process, the heating field fades and the crystal cools down mostly accompanied by stress-induced generation of new dislocations in the vicinity of the upper “tail.”

s0035 6.1.3 Crucial FZ Details

s0040 6.1.3.1 *Origin and Analysis of Failures*

p0110 The growth of dislocation-free silicon FZ crystals is rather sophisticated especially in view of large-diameter crystals. FZ runs can fail accidentally by, for example, dust particles in the growth surroundings, ground vibrations, or structural anomalies of the feed rod, or, systematically, by inconvenient growth conditions like wrongly chosen RF power, pull or rotation values, and inappropriate design or adjustment of the inducting coil that can cause inapplicable temperature and stress anomalies in the crystal or electrodynamic forces destabilizing the melt zone. It is quite advantageous that the FZ process can be well visually observed. However, it is almost impossible to clarify the real reasons of failures because most in situ measurements are impossible. Therefore, structural and electrical diagnostics of the grown crystal are essential for process evaluation and optimization.

p0115 The crystallization interface as a distinct isothermal face, in particular its deflection, gives information about the temperature and stress fields' overall growth phases, and its shape is generally used for the validation of numerical models. This can be determined from the striation pattern in the grown crystal, which can be well detected on axially cut samples by evaluation of the doping or rather the resistivity distribution using the lateral photovoltage scanning (LPS) method [7] (Figure 6.7). Here, a scanning laser focus

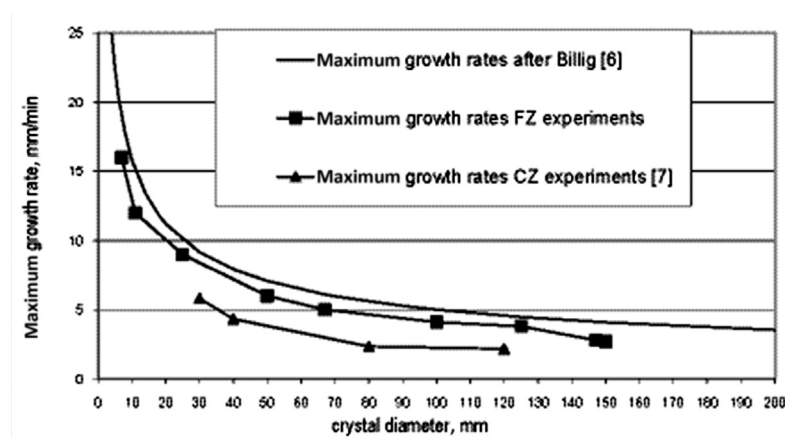


f0040 **FIGURE 6.7** Lateral photovoltage scanning plot of an axially cut sample from a silicon single crystal showing solid liquid interface curves and resistivity variations.

generates a small voltage signal between opposite sample rims corresponding to the lateral gradient of the doping concentration. Besides the interface curve, the LPS plot contains information about resistivity fluctuations originated by crystal rotation as well as by the time-dependent melt flow field responsible for the radial resistivity profile and its variations.

s0045 6.1.3.2 Rotation and Pull Rates

p0120 FZ crystals grow in relatively cold surroundings causing high temperature gradients at the crystallization front. Therefore, compared with the CZ process, higher pull rates are possible. [Figure 6.8](#) shows experimentally determined values of the maximum pull rates for dislocation-free FZ crystals depending on the diameter [8]. With their FZ technique, the authors reached pull rates of about 75% (CZ: c. 50%) of the thermotechnically



f0045 **FIGURE 6.8** Maximum growth rates for floating zone silicon compared to Czochralski silicon and the theoretical limit calculated by Billig [9].

10 HANDBOOK OF CRYSTAL GROWTH

determined upper limit calculated by Billig [9] for crystal diameters of 10–150 mm corresponding to the maximum pull rates for a dislocation-free FZ growth of 17 mm/min to 3 mm/min, respectively.

p0125 The necessary feed rate is determined by the silicon mass balance as crystal pull rate multiplied by the squared ratio of the diameters of crystal and feed. However, there are limitations. On one hand, a high feeding rate lets the distance shrink between the induction coil and the melting front of the feed rod that could touch each other; on the other hand, too low melting rates cause a rough melting front, and, as a consequence, skin-effect related silicon “noses” are formed that cannot be inductively removed as shown in Figure 6.9. This and other effects limit the relative deviation between the diameters of crystal and feed rod empirically to c. $\pm 25\%$.

p0130 Generally, feed and crystal rotate in order to improve the thermal symmetry, but furthermore, the rotation affects the process.

p0135 If the feed rod rotates with c. 2–4/min, “noses” can appear. Therefore, lower rotation rates are preferred.

p0140 On one hand, high crystal rotation rates lower the radial resistivity variation (RRV) and the deflection of the growth interface by homogenizing the dopant concentration as well as the temperature in the melt; on the other hand, the centrifugal forces act against the surface tension and destabilize the melt meniscus and following crystal morphology. This double bind can be overcome if the comparably fast crystal rotation is periodically reversed. Specially designed schemes of rotation modulation are patented [10].

s0050 6.1.3.3 Stability of the Molten Zone and Growth Angle

p0145 For a successful FZ growth, the molten zone must be in equilibrium of all acting forces originated mainly by surface tension, electrodynamics, inertia, and gravity. Furthermore, the equilibrium has to be dynamically stable, i.e., it has to steadily come back to the equilibrium by itself after mechanical deviations. The isostatic melt pressure corresponding to the degree of filling of the molten zone in relation to its diameter and height



f0050 **FIGURE 6.9** Formation of a “nose” that cannot be molten inductively and can lead to a process crash.

is most relevant for the stability, but hardly measurable, and will be discussed in the next sections. Instability of the zone is generally followed either by spilling out of the melt (too much melt) or by zone separation (too little melt).

p0150 Visible indications of an upcoming loss of the zone stability is the melt neck diameter in relation to the zone height, e.g., the vertical distance between upper and lower interface lines and the meniscus shape or rather the angle between the melt meniscus and the crystal surface at the crystallization interface. For a safe crystal growth, this angle appears to be relevant to avoid deviations of the so-called growth angle.

p0155 However, even a stable molten zone does not ensure a successful dislocation-free growth. The time-depending thermomechanical shear stress in the crystal must generally be limited, but cannot be quantitatively specified today.

p0160 If the crystal grows stationary with a constant diameter, the angle between the tangents to the melt surface and the crystal surface at the position of the crystallization interface is commonly not zero and depends only on material parameters. It was experimentally determined for several substances from photographs of melt zones. This growth angle for silicon was recently determined to be $11.5^\circ \pm 1.9^\circ$ [11].

s0055 6.1.3.4 The Feed Rod

p0165 The almost cylindrical silicon feed rod, which has to be controlled molten inductively, is commonly produced after the so-called Siemens process by pyrolytic deposition of either trichlor silane SiHCl_3 or mono silane SiH_4 on electrically heated silicon filaments (slim rods). Sometimes, feed rods are used that were solidified from the melt after techniques like CZ, directional solidification, continuous crystallization, or previous FZ purification runs.

p0170 The purity of the feed rod influences the purity of the grown FZ crystal, which is generally improved by segregation. Especially transition metals with segregation coefficients $k \ll 1$ are effectively depleted, whereas the important dopants boron ($k = 0.8$) [AU2] and phosphorus ($k = 0.36$) are rather evenly distributed, which facilitates axially homogeneous doping techniques.

p0175 The crystalline structure of the feed rod is not implicitly important, but thermal and electrical properties should be homogeneous, at least free of anomalies like cavities, cracks, and resistant microinclusions like SiO_2 or SiC.

p0180 The surface roughness of the rod should approximately be below 1 mm. If necessary, it can be ground. Normally, the feed rod needs to be shaped for the FZ process by grinding [AU3] a cone on one end as well as mounting grooves on the other end. Before assembling, the feed rod must be carefully cleaned by etching off a few microns from the surface with a mixture of nitric and hydrofluoric acid followed by rinsing with ultra pure water.

s0060 6.1.3.5 Induction Coil and Arcing

p0185 Of course, all other items of the FZ setup positioned near the hot zone must also be cleaned carefully. Especially the surfaces of the induction coil made of copper or silver should be brightly polished and freshly cleaned in an ultrasonic bath.

12 HANDBOOK OF CRYSTAL GROWTH

p0190 The coil is electrically and mechanically connected with the RF power generator outside the growth chamber via the coaxial feedthrough, even supplying the coil with water. It is a very sensitive component because, here, the highest voltages occur and surface damage or pollution could initiate electrical breakthrough.

p0195 However, most critical for electrical breakthrough or arcing is the slit of the inductor. In fact, this is not the region of maximum RF voltage but of the highest electric field strength due to the narrow gap, which has to be minimized in order to reduce a heating peak under the slit causing local stress near the growth interface. Arcing and stress anomalies are the worst drawbacks against increasing the crystal diameter. Unfortunately, most approaches to prevent that arcing lead to double binds:

- u0010 • Reduction of the electric field strength by widening the slot is coupled with increasing deviations of the thermal symmetry, causing dislocations.
- u0015 • Increased pressure of the growth atmosphere accelerates the convective cooling of the crystal, causing hazardous thermal stress and the risk of crystal cracking or at least dislocation generation.
- u0020 • A lower working frequency corresponds to lower RF voltages at the coil but increases the Lorenz forces driving the melt convection [12]. Additionally, the enlarged skin depth disturbs the melting of the feed rod.
- u0025 • Adding traces of nitrogen increases the electric strength of the argon atmosphere, but too much nitrogen causes silicon nitride precipitates.

s0065 6.1.4 FZ Crystal Morphology: Ridges and Orientation

s0070 6.1.4.1 Growth Habitus

p0220 Indeed, the crystal anisotropy of silicon concerning the most material parameters is non-
[AU4] negligible but comparably weak due to the fully covalent bonds and the high symmetry of the face-centered cubic lattice, but FZ silicon crystals grow under thermal conditions, which are not homogeneous but of almost rotational symmetry that dominate their habitus. Both the axisymmetric temperature gradient and the surface tension tend to form a circular crystal cross-section and a cylindrical shape, which is not completely perfect in reality. If the radial temperature gradient is too weak combined with an imperfect thermal symmetry, e.g., due to inductor issues, the growth interface easily becomes inclined, which deforms the melt meniscus and causes eccentric crystal growth. The interaction with the rotation then affects a corkscrew-like habitus, being a fatal risk for the crystal.

p0225 Additionally, typical ridges appear along specific cylinder surface lines according to the respective crystallographic growth direction because the temperature of solidification slightly depends on the local orientation of the curved crystallization front. As a result, the radial crystallization rate differs when generating those ridges. Watching the ridges, the crystal grower can directly realize the crystal orientation and the loss of the dislocation-free structure.

- p0230 In case of the $\langle 100 \rangle$ growth direction, four equal ridges appear mutually twisted by an angle of 90° according to the fourfold axial symmetry. These ridges are commonly weak and do not disturb the thermal symmetry. On the other hand the threefold $\langle 111 \rangle$ direction corresponds to three larger ridges twisted by 120° and three weaker ones in between. The $\langle 111 \rangle$ ridges often transform to different bulges causing eccentric distortions of the temperature and stress fields (see [Figure 6.1\(a\)](#)).
- p0235 [AU5] Other orientation-related peculiarities are based on different angles between crystal axis and the main plains for dislocation gliding and cleavage, which are influencing the probability of dislocation generation and crystal bursting during FZ growth, respectively.
- p0240 For these reasons, $\langle 111 \rangle$ FZ crystals can currently be grown with a maximum diameter of 150 mm, whereas $\langle 100 \rangle$ crystals reach 200 mm.

s0075 6.1.5 Doping Techniques and Impurity Distribution

- p0245 The classical doping method for FZ silicon is the use of pre-doped feed rods produced after the Siemens process (see [Section 6.1.3.4](#)) using intentionally doped slim rods that define the resistivity and the conduction type of the resulting FZ crystal. This method is rather simple and axially homogeneous but not flexible.
- p0250 Presently, FZ crystals are mostly doped in situ by a controlled gas stream containing traces of gaseous compounds of the doping elements (PH_3 or B_2H_4), which is blown directly onto the molten zone, where the compound decomposes and the remaining dopants P or B dissolve and spread homogeneously by melt convection. However, the doping concentration varies radially because the melt flow field influences the thickness of the diffusion layer close to the crystallization interface.
- p0255 For dopants with small segregation coefficients $k \ll 1$ like Ga, In, or Al, a piece of highly pre-doped silicon (“doping pill”) can be put in a small radial hole that has been drilled into the feed rod. When molten, the pill will dope the melt. During the FZ growth, the doping concentration in melt and crystal will stay almost constant because a tiny but constant fraction of the dopant will be dissolved in the crystal.
- p0260 Doping with oxygen from the gas phase is not effective because mainly gaseous SiO evaporates, but by contacting the melt surface with a slice of fused silica (SiO_2), oxygen (but no carbon) is introduced according to the contact area similar to the CZ process [13].

s0080 6.1.6 Recent Development

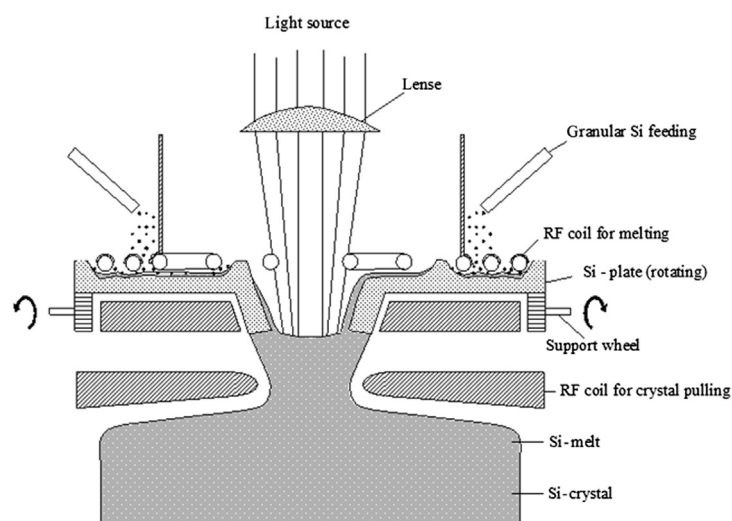
- p0265 FZ silicon has some benefits in comparison to CZ silicon. It features some superior material parameters, and the FZ process saves energy and avoids consumables like crucible, heaters, and thermal insulation. However, its field of application is restricted mainly by the expensive high quality feed rods and the limitation of the diameters of the Siemens feed rods and the FZ crystals.
- p0270 Recently, a novel crystal growth concept was investigated with the goal to grow cost-reduced crystals of FZ quality by replacing the feed rod with continuously fed fluid bed granulate, which is produced by the Siemens process with excellent purity and only a

14 HANDBOOK OF CRYSTAL GROWTH

fraction of the effort necessary for polysilicon rods. For this granulate FZ (gFZ) method, the German company Siltronic AG applied several patents [14] concerning the process principle and special induction coils as shown in Figure 6.10. The Si granulate is continuously supplied to a plate made of silicon being heated by a sophisticated inductor, which simultaneously melts the granulate and sustains a tubular opening in the center of the silicon plate, where the melt can pass down by forming a hanging neck as a bridge to the melt lake on top of the growing gFZ crystal. This silicon plate must be cooled from the bottom to protect it against distortion. As a consequence, a second independent inductor is installed on top of that Si melt lake in the gap under the cooled Si plate. This lower induction coil has to maintain the thermal field for the crystal, which grows like in the FZ process. If the gFZ method is matured, silicon crystals of FZ quality can be produced with reduced costs and could compete even against CZ silicon particularly for high efficiency solar modules.

p0275 Another new attempt also targets PV application: the growth of FZ crystals with quadratic cross-section (qFZ) [15]. In principle, the qFz crystal grows without rotation in a heating field of fourfold symmetry provided by a special inducting coil [16]. The feasibility of that concept was demonstrated for a 100 mm × 100 mm cross-section. Because solar cells are quadratic, the waste of silicon is reduced if the crystal is quadratic. Furthermore, the needed RF voltage mainly depends on the crystal cross-section, larger squares can be grown before arcing occurs.

p0280 Electric breakthrough at the coil slit is still the most crucial drawback for the FZ development toward diameters beyond 200 mm. The application of lower working frequencies resulting in an approximately linearly decreasing voltage could be promising, but negative side effects might be difficult to overcome.



f0055

FIGURE 6.10 Principle of the granulate floating zone method.

p0285 A detailed understanding of the gas-discharge processes under the specific FZ conditions appears as the key for substantial progress. It is presently not well understood why the RF breakthrough voltage only weakly increases with increasing pressure of the growth atmosphere and not linearly as predicted by the Paschen rule [17]. Especially the impact of the gas temperature in the vicinity of the cooled coil, where the temperature difference to the melt is more than 1000 K over a few mm distance, should be investigated in detail.

s0085 6.2 Automation of the Floating Zone Process Using Model-Based Control

s0090 6.2.1 Motivation

p0290 For increasing the yield of dislocation-free monocrystals, attempts are being made to make the FZ process automatic. The large silicon crystals of up to 200 mm diameter, as grown in the modern industrial FZ production, require sophisticated process conditions. Even for experienced operators, it is difficult to keep the small window of suitable growth conditions by manual growth. Therefore, automatic growth control is a key issue in production of monocrystalline silicon with respect to yield, quality, and reproducibility. It is essential to produce crystals with equal properties by keeping identical processing conditions.

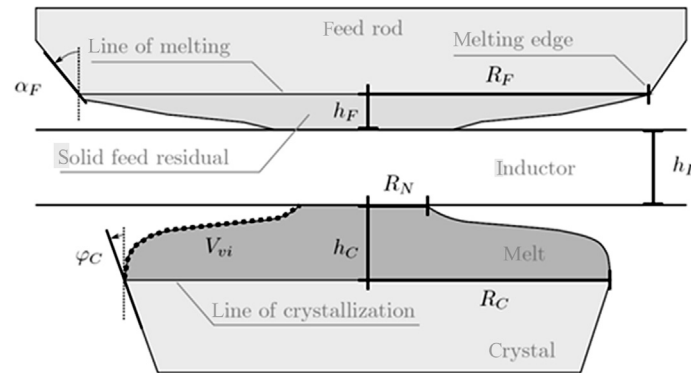
p0295 In the 1980s, in the FZ industry, the application of automatic control, mainly PID controllers, was targeted [18–20]. Reference values are crystal diameter and axial height of the molten zone. The process is monitored with an imaging device, and geometric quantities are measured from the obtained video camera images. The controller parameters are set up separately for each setup in every process phase due to the changing dynamics during the process. If the process environment is modified (new machine components, new crystal diameter), the PID controller has to be set up again. The better way is a model-based controller that gives a widely flexible handling of different machine components, different inductor types, and different target diameters. Also, the changing dynamics of the process can be directly handled by model-based automation if a suitable mathematical model is available. In 1996, the German company Wacker Siltronic AG published an idea to control growth processes, for instance, CZ and FZ, by a prediction control method (see [21,22]). The patents do not provide a model description, they include the idea of predictive control by using online and offline simulation. Due to the complex dynamics, it is necessary to use a nonlinear model for controlling the crystal growth of large-diameter crystals. In this section, a nonlinear model predictive control (NMPC) is presented to control the process as developed in the Leibniz Institute for Crystal Growth (IKZ) by Werner [23].

s0095 6.2.2 Description of the Measurement System

p0300 The growth chamber has an optical access to the FZ process through a quartz window, so that the geometrical quantities of feed rod, molten zone, and crystal can be obtained

16 HANDBOOK OF CRYSTAL GROWTH

f0060 **FIGURE 6.11** Geometrical quantities calculated from measurements: visible melt volume V_{vi} , crystal radius R_C , crystal angle φ_C , feed radius R_F , feed angle α_F , upper zone height h_F , lower zone height h_C , height of the inductor h_I , radius of the melt neck R_N .



by visual image processing. Figure 6.11 shows a sketch of the geometrical quantities calculated from measurements. The identification of the quantities is based on the idea of edge detection, a mathematical method to identify points in a digital image. The points are characterized by a sharp change of the image brightness [24]. The crystal radius R_C is directly measured at the line of crystallization (solid–liquid interface). The lower zone height h_C is the distance between the lower edge of the inductor and the line of crystallization. The volume of the molten zone consists of a visible and a hidden part. The visible melt volume V_{vi} is calculated from the outer contour of the molten zone assuming rotational symmetry. The volume V_{bo} of the melt bowl is covered by the crystal surface and arises due to the radial temperature gradient in the crystal. An approximation of V_{bo} based on LPS is given in Ref. [23]. Instead of the real melt neck, which is covered by the inductor, an approximated R_N is measured directly below the inductor. The upper zone height h_F is the distance between the upper edge of the inductor and the line of melting. The solid part below the line of melting is the feed residual. The feed rod is shaped at the lower end, so, it is required to measure radius R_F and angle α_F of the feed rod. The distance between the lines of melting and crystallization is the height of the full zone h_C .

p0305 [AU6] The melting rate v_{Me} and the crystallization rate v_{Cr} are not directly measurable and have to be identified using an estimator. The melting rate $v_{Me} = -\dot{L}_F$ is defined as negative derivative of the feed rod length L_F (distance between line of melting and feed holder). A positive melting rate v_{Me} means a decreasing feed length. The crystallization rate $v_{Cr} = \dot{L}_C$ is the derivative of the crystal length L_C (distance between line of crystallization and crystal holder). In the literature, the crystallization rate is also denoted as the growth rate.

s0100 6.2.3 Modeling of the Floating Zone Process

p0310 The goal is to get a set of nonlinear differential equations of first order with respect to time, which predicts the fundamental behavior of the process dynamics without

expensive and time-consuming calculations. The model based on physical conservation laws and details is given in Ref. [23]. The model describes the dynamical behavior in the mathematical form

$$\dot{\underline{x}}(t) = f(t, \underline{x}(t), \underline{u}(t), \underline{\Theta}) \quad \text{with} \quad \underline{x}(0) = \underline{x}_0. \quad (6.2)$$

p0315 For a given initial state \underline{x}_0 and a given sequence of inputs $\underline{u}(t)$, the future development of the state vector $\underline{x}(t)$ can be calculated by using a numerical integration of the state derivatives $\dot{\underline{x}}(t)$. The elements of the parameter vector $\underline{\Theta}$ represent the model parameters. The state vector $\underline{x}(t)$ includes the components: radius of feed R_F and crystal R_C height of upper zone h_F and lower zone h_C angle at feed α_F and crystal φ_C , volume of visible melt V_{vi} , radius of melt neck R_N , crystallization rate v_{Cr} , melting rate v_{Me} , and inductor power P_{ind} . The input vector $\underline{u}(t)$ includes the three components: generator power P_{gen} , pull rate of feed v_F , and crystal v_C . The following differential equations are involved:

$$\frac{d}{dt}(R_F) = v_{Me} \cdot \tan(\alpha_F), \quad (6.3)$$

$$\frac{d}{dt}(R_C) = v_{Cr} \cdot \tan(\varphi_C), \quad (6.4)$$

$$\frac{d}{dt}(h_F) = v_{Me} - v_F, \quad (6.5)$$

$$\frac{d}{dt}(h_C) = v_C - v_{Cr}, \quad (6.6)$$

$$\frac{d}{dt}(\alpha_F) = 0, \quad (6.7)$$

$$\frac{d}{dt}(\varphi_C) = \frac{\Delta\varphi_C}{\Delta V_{vi}} \dot{V}_{vi} + \frac{\Delta\varphi_C}{\Delta R_C} \dot{R}_C + \frac{\Delta\varphi_C}{\Delta h_C} \dot{h}_C + \frac{\Delta\varphi_C}{\Delta R_N} \dot{R}_N, \quad (6.8)$$

$$\frac{d}{dt}(V_{vi}) = \frac{\rho_S}{\rho_M} (\pi R_F^2 v_{Me} - \pi R_C^2 v_{Cr} - \dot{V}_{fr}) - \frac{\rho_M - \rho_S}{\rho_M} \dot{V}_{bo}, \quad (6.9)$$

$$\frac{d}{dt}(R_N) = n_h (\dot{h}_F + \dot{h}_C), \quad (6.10)$$

$$\frac{d}{dt}(P_{ind}) = \frac{1}{\tau_p} (K_p \cdot P_{gen} - P_{ind}), \quad (6.11)$$

$$\frac{d}{dt}(v_{Me}) = \frac{d}{dt} \left(\frac{P_F - P_{F,loss} + q_0 \rho_S \dot{V}_{fr}}{q_0 \rho_S \pi R_F^2} \right), \quad (6.12)$$

$$\frac{d}{dt}(v_{Cr}) = \frac{d}{dt} \left(\frac{P_{C,loss} - P_C + q_0 \rho_S \dot{V}_{bo}}{q_0 \rho_S \pi R_C^2} \right). \quad (6.13)$$

where ρ_M is the density of the melt, ρ_S is the solid density, \dot{V}_{fr} is the derivative of the volume of the feed residual, \dot{V}_{bo} is the derivative of the volume of the melt bowl, q_0 is the latent heat. The variables n_h , K_p , τ_p are model parameter. The terms $P_{F,loss}$ and $P_{C,loss}$ describe the power loss of feed rod and crystal due to radiation. The power introduced into feed rod P_F and crystal P_C are modeled as functions of inductor power P_{ind} ,

18 HANDBOOK OF CRYSTAL GROWTH

corresponding radii R_F and R_C , corresponding zone heights h_F and h_C , and further model parameters. A detailed description is given in Ref. [23].

s0105 6.2.4 Choice of Reference and Manipulated Variables

p0320 It is essential to set up suitable reference and control variables to fulfill the requirements of the FZ process. In the presented automation concept, the considered control variables are the heater power of the inductor and the pull rates of feed and crystal.

s0110 6.2.4.1 *Creating the Thin Neck*

p0325 This is the start of growing a crystal. Feed and crystal are moved downward to create the thin neck. The crystal diameter of 5–6 mm, resulting from the diameter of the seed, has to be reduced down to 2–3 mm and kept constant until the end of that phase where all dislocations have to grow out. For creating the thin neck, the references are zone height and crystal diameter as functions of time.

s0115 6.2.4.2 *Growing the Crystal Cone*

p0330 The crystal diameter has to be increased by producing and keeping a melt overhang by adjusting heater power and pull rate of the feed rod. In this phase, a constant or slowly changing pull rate of the crystal is used to ensure the dislocation-free growth. The observation of the melt neck is important to satisfy the limits due to the inductor hole. To overcome measuring problems of the melt neck, the zone height h_C is applied as an auxiliary quantity within the automation. The reference of the zone height has to be designed for a suitable melt neck. The complete crystal, starting from the cone, can be defined as a function of the crystal length L_C for achieving a reproducible crystal shape.

s0120 6.2.4.3 *Growing the Cylinder*

p0335 Here, the crystal diameter is held constant. This is managed by constant heater power and constant pull rates of feed and crystal. The process is self-regulating and in a stable state during this phase. At the end of the process, the heater power has to be adjusted slightly to keep the height of the molten zone. Here, the heat transport of the feed rod is affected due to its length reduction.

s0125 6.2.5 Regulated Growth of the Avogadro Crystal

p0340 As an example of applying this control method, the regulated growth of a crystal with a special shape, the so-called Avogadro crystal, is shown. The crystal is used in an approach to determine the Avogadro constant by “counting” the atoms of a 1 kg monocrystalline sphere of ^{28}Si isotope. Details of the physical background are given in the reviews [25–27]. Two silicon spheres have to be obtained from one grown crystal. Due to the high costs of the material, a regulation is applied to grow a crystal with minimum material waste. So, there is no cylindrical part in the crystal. The diameter has to be decreased after finishing the cone and increased again up to the full diameter.



f0065 **FIGURE 6.12** Image of the grown Avogadro crystal using regulation. The image was taken by Turschner at the Leibniz Institute for Crystal Growth (IKZ).

A regulation is needed to fulfill this reference of the shape. For this experiment, a common feed rod of polycrystalline silicon is used instead of the expensive ^{28}Si material. The automation starts at a crystal diameter D_C of 42 mm. [Figure 6.12](#) shows the image of an “Avogadro crystal.” The advantage of applying the model predictive control, instead of the previously used PID control, is that this shaped crystal can be grown at other FZ machines without a new parameter identification.

s0130 6.3 Mathematical Modeling of the Floating Zone Silicon Growth

s0135 6.3.1 Introduction

p0345 The numerical simulation of the FZ process is mainly carried out to understand the physics of the process and to support its development. The simulation considers the most important physical effects that connect the process parameters to quality, shape, and yield of the grown crystals and to the ability to grow the crystal at all. Nowadays, models of the FZ process can predict the effects quantitatively and are successfully used in the process development.

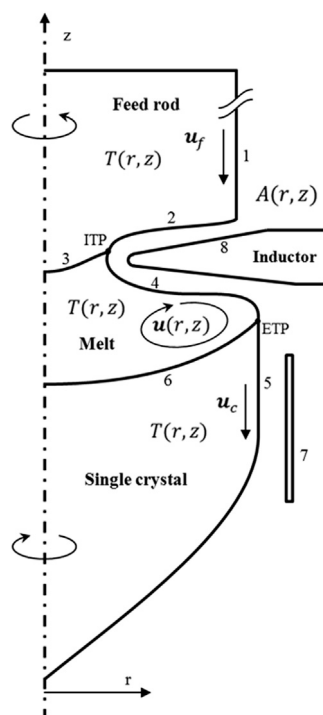
p0350 This section describes the needle-eye FZ process from the modeling point of view, gives an overview of the modeling history, outlines the state-of-the-art model system,

20 HANDBOOK OF CRYSTAL GROWTH

and presents modeling results characterizing the most important findings and the effects of process parameters.

p0355 Due to the absence of a crucible, all melt interfaces are determined by the machine setup, process parameters, and the process history, but not by a predefined geometry of the crucible. This requires a global model for the calculation of the interface shapes considering the electromagnetic (EM), thermal, and flow fields.

p0360 The RF inductor (Figure 6.13) induces the EM field into the Si material at all surfaces that are in contact with the process gas, mainly in the feed rod and in the melt. As a result, the feed rod is molten and the so-called open melting front 2 is formed. A part of the induced heat is radiated away from the open melting front directly and the rest is conducted through the feed rod to its cylindrical surface 1 and radiated away there. The heat sources at the free melt surface 4 keep the zone molten, compensating the radiation heat loss and ensuring some heat flux and thermal gradient at the crystallization interface 6 and melting interface 3. The induced Lorenz forces influence the shape of the free melt surface and contribute to the convection in the molten zone. Aside from the EM forces, the shape of the free surface is determined by the hydrostatic pressure and the surface tension. The free surface contacts the crystal at exterior triple point (ETP) and the poly rod at internal triple point (ITP). The shape of the crystallization interface is



f0070 **FIGURE 6.13** Schematics of the floating zone model. 1, cylindrical surface of feed rod; 2, open melting front; 3, melting front; 4, free melt surface; 5, cylindrical crystal surface; 6, crystallization interface; 7, reflector; after [28].

determined mainly by the heat flux from the melt and by the radiation on the crystal surface 5, which is sometimes reduced using a reflector.

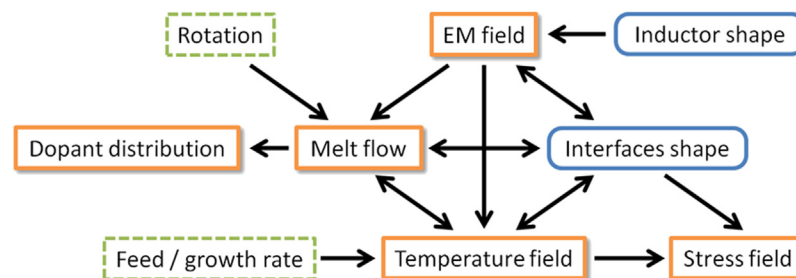
p0365 The EM and temperature fields are strongly coupled with the interface shapes and a change of some process parameter will influence all of them, see Figure 6.14. Therefore the modeling of particular processes without the use of a global model is questionable and should be handled with care, if some a priori shapes are used, also experimentally obtained ones.

s0140 6.3.2 Historical Overview

p0370 The first article on modeling of the needle-eye FZ growth process was published in 1983 by Mühlbauer et al. [28]. The current distribution at the free melt surface and the electromagnetically driven flow in the melt were calculated assuming a predefined interface. Later articles in the early 1990s were also devoted to the modeling of the EM field [29]. The shape of free surface and distribution of electric current for predefined triple points were calculated by Lie et al. in Ref. [30] and the melt motion under the influence of a strong axial magnetic field in Ref. [31]. The 3D distribution of the EM field was calculated by Mühlbauer et al. in Refs [32,33]. Despite a considerable asymmetry as shown in these articles, axisymmetric 2D models were widely used to reduce the computational effort. The effect of the inductor slits on the current distribution is considered in 2D models in a simple [34] and advanced way [35].

p0375 The first global 2D model considering the EM, temperature, and transient fluid flow fields as well as the interface shapes was published by Mühlbauer et al. [29] and investigated in detail in Ref. [34]. Riemann et al. calculated the shapes of the free surface and the crystallization interface, and the thermal stress in the crystal [36]. Mühlbauer et al. extended the model [34] and calculated transient dopant transport in the melt [37] and compared the calculated resistivity distributions with experiments [38,39]. The influence of different additional magnetic fields on the resistivity distribution is studied by Raming et al. in [40–42].

p0380 Other global models were developed in the late 1990s. Togawa et al. [43] calculated the interface shapes, heat transfer, a transient melt flow including dopant transport, and



f0075 **FIGURE 6.14** Schematic of the coupling between the modeled physical fields (solid rectangles), the interface shapes (rounded rectangles), and the influence of process parameters (dashed rectangles).

22 HANDBOOK OF CRYSTAL GROWTH

the resistivity distribution. This model is improved with implemented radiation view factors by Guo et al. [44]. Larsen et al. [45] calculated interface shapes, heat transfer, and point defect dynamics in 4" and 0.8" crystals. The dopant transport for 4" processes is modeled in Ref. [46].

- p0385 Muiznieks et al. [47] showed that the thermal stress in 4" FZ crystals is higher than in 300 mm CZ crystals and investigated the dislocation generation induced by thermal stress.
- p0390 The model [34] is reconsidered, rewritten, and extended by the view factor radiation and the variable liquid film thickness on the open melting front by Ratnieks et al. [48,49]. Next model extension by Rudevics et al. [50–52] allows calculating the FZ process in a transient way, the growth of starting and end cones, as well as the control of the crystal diameter using PID algorithm.
- p0395 A coupled 3D model for the EM, temperature, melt flow, and dopant concentration fields was developed for the first time by Ratnieks et al. [53]. Here and in further studies [54–56] the generation of the rotational striations in the crystal were shown. The paper [57] shows that the resistivity fluctuations due to convection are at least by one order of magnitude higher than those due to the changes of the local growth velocity.
- p0400 The 3D resistivity distribution is investigated under the impact of rotating [58–60] and steady axial [59] magnetic fields.
- p0405 A model for the simulation of an EM field, heat transfer, melt flow, and thermal stress was developed and presented in the PhD theses of Assaker [61] and Bioul [62].
- p0410 Rudevics et al. [63] presented a nonsymmetric 3D model calculating EM and temperature fields as well as the free melt surface and crystallization interface based exclusively on boundary element method (BEM).
- p0415 3D modeling of the free melt surface and crystallization interface during the growth of square-shaped FZ crystals is presented in Ref. [64].
- p0420 Menzel [65] uses the measured interface shapes to calculate the 3D EM field of different frequencies using the commercial code SINGULA and applying these results for the calculation of 2D fluid flow using the commercial code ANSYS-CFX.
- p0425 Wünschler et al. [66] and Menzel [12] applied COMSOL for 3D and 2.5D modeling of EM, temperature, and stress fields as well as the shapes of free surface, melting, and crystallization interfaces for 4" and 5" process.
- p0430 The effect of gas flow on the cooling of the crystal is considered by applying a heat transfer coefficient in Refs [12,46].

s0145 6.3.3 Mathematical Models

- p0435 The models described here build the core system necessary to satisfy the interests of crystal growers developing the process regarding increased quality and yield requirements. The models are macroscopic, i.e., they consider the material with continuum properties and do not describe the atomistic scale of crystal growth. However, the calculated quantities can be further used to analyze the processes on micro and atomistic scales [67].

p0440 The conditions near the molten zone during the growth remain very similar for a long time, therefore, mainly the quasi-steady approach is used (the non-steady model is described in [Section 6.3.3.7.](#))

p0445 The crystal, poly rod, and the melting and crystallization interfaces are assumed axisymmetric in all models because the rotation averages the influence of the nonsymmetric one-turn inductor (except for growth of square-shaped crystals [\[64\]](#)).

p0450 The schematic of main influences coupling the modeled physical fields, the interface shapes, and the process parameters is shown in [Figure 6.14](#). The interface shapes depend on the EM, temperature, and melt flow fields, and vice versa. Therefore, any modeling study of one of the particular fields demands the coupled modeling of the interface shape. The following sections describe first the particular models assuming fixed interfaces, and [Section 6.3.3.5](#) reports on the coupling procedure in more detail. Afterward the specifics of transient modeling are described.

s0150 6.3.3.1 *Electromagnetic Field*

p0455 The EM field heats up and melts the polycrystalline rod as well as maintains the molten zone from which the crystal is grown. As the EM field distributes with the speed of light and its frequency is several orders higher than the time scale of the thermal and mass transport processes, all other fields and interfaces can be assumed to be fixed during the calculation of the EM field. At the typical frequency of 3 MHz the EM field penetrates into the thin skin layer of 1.3 mm in solid Si, 0.27 mm in molten Si, and 0.04 mm into the Ag inductor. The rest of the conducting bodies are free from the EM field. Using Maxwell's equations in quasi-static approximation, where the displacement current is neglected [\[68\]](#) in the formulation of the magnetic vector potential the Laplace equation in a nonconducting space is

$$\Delta A = 0. \quad (6.14)$$

p0460 Assuming that all currents can be described by surface currents, the boundary condition (BC) for the vector potential on Si surfaces is

$$A = 0 \quad (6.15)$$

and on the inductor surface it is defined by the applied voltage [\[34\]](#). The distribution of currents is searched to fulfill [Eqn \(6.15\)](#). It is solved using BEM, therefore only surface meshes in 3D space are necessary. The result is the distribution of the effective surface current density j_s . For more detail on the 2D case and the 2D slit model see Ref. [\[35\]](#), and for the 3D case formulation see Ref. [\[33\]](#). From the surface current density j_s the normal EM pressure for the calculation of the free surface shape, the tangential EM surface force for the melt convection, and the Joulean heat sources for the temperature field can be calculated [\[35\]](#).

s0155 6.3.3.2 *Temperature Field*

p0465 Due to inductive heating, the highest temperature in the FZ system is in the melt. Therefore, the temperature for the crystal and the melt ambient is lower than in the CZ

24 HANDBOOK OF CRYSTAL GROWTH

system and the temperature gradients are higher. The heat transport is characterized by Joulean heat sources at Si surfaces, by conduction in a poly rod and a crystal, and by conduction and convection in the melt as well as radiation in the gas.

p0470 The temperature transport equation in solids using the quasi-stationary approach is

$$\rho c_p \mathbf{u}_c \text{grad } T = \text{div}(\lambda_s(T) \text{grad } T) \quad (6.16)$$

where \mathbf{u}_c is the vertical pull rate of the feed or the crystal with respect to the laboratory reference system. The interfaces' shape is assumed to be fixed during the calculation of the temperature field. Surface heat sources are not included in Eqn (16) but are considered in the BC. The temperature on the melting, crystallization, and free melting front is set to melting temperature T_0 . On Si–gas interfaces the heat flow BC is set to

$$\lambda_s(T) \frac{\partial T}{\partial n} = q^{EM} - q^{rad}, \quad (6.17)$$

where q^{EM} are the Joulean heat sources and q^{rad} are the radiation heat losses described in the next section. Heat transfer is modeled by finite element method (FEM). The calculated temperature fields are used for the calculation of interface shapes and the thermal stress.

p0475 The radiation in ambient gas is the main heat transfer mechanism from the hot crystal, melt, and poly rod surfaces to the cold recipient and inductor, the conduction and convection effects in the gas are less important [12]. The simplest assumption is the radiation to predefined ambient temperature T_a

$$q^{rad} = \varepsilon \sigma_{SB} (T^4 - T_a^4). \quad (6.18)$$

p0480 Lower ambient temperature for crystal and poly rod and higher for melt and open melting front are applied [34].

p0485 Later the radiation heat exchange is calculated more precisely using view factors describing the gray diffuse radiation exchange in transparent media; see Ref. [44] for differences between the results using constant ambient temperature and view factors. Details about the calculation of view factors can be found in Ref. [35]. The calculation of view factors is a time-consuming operation in the 3D [63] and also in the 2D axisymmetric case [69] and is often optimized at the expense of precision [35].

s0160 6.3.3.3 Melt Flow

p0490 The melt flow in the FZ process is laminar but nonstationary [28]. The continuity equation for an incompressible fluid and the Navier–Stokes equation using the Boussinesq approximation including the external force, e.g., due to an applied steady or low frequency magnetic field, are solved. Marangoni forces due to the temperature dependence of surface tension and EM forces caused by the RF inductor are included in the BC on the free melt surface [35,70] shows that it is allowable. The rotation of the crystal and the poly rod causes forced convection and the corresponding velocities are also included in the BC.

p0495 The temperature distribution in the melt is described by the heat transfer equation and is coupled to the Navier–Stokes equation. Joulean heat sources are included in the BC similarly as in the solid parts.

p0500 In the 2D case model equations can be rewritten in the vorticity-stream function ($\omega - \psi$) formulation and can be solved using FEM as described in detail in Refs [34,35]. Three dimensional laminar unsteady model equations are solved based on the OpenFOAM libraries [71,72].

s0165 6.3.3.4 Impurity Distribution

p0505 Concentrations of impurities (dopants) in the Si melt are small, therefore, they have no influence on the flow. The conservation equation of dilute species C is

$$\frac{\partial C}{\partial t} + (\mathbf{u}\nabla)C = D\Delta C \quad (6.19)$$

where D is the diffusion coefficient of dopants in molten Si. The segregation BC is set at the crystallization interface [73]. If the doping is realized from the feed rod, the concentration C at the melting front is set equal to the concentration of the dopants in the feed rod [40,41,46] and zero flux is set to the free melt surface [37]. In the case of doping from gas, the concentration is set to zero on the feed rod and is normalized to 1 at the free surface [74] or constant flux is set at the free surface [46]. The different conditions at the free surface are used because the precise transport of dopants in the gas is not modeled.

s0170 6.3.3.5 Shape of Interfaces

p0510 The shapes of melting and crystallization interfaces are defined by the balance of heat fluxes. The BC for temperature is set to $T = T_0$ during the calculation of the temperature field in each part (poly rod, melt, crystal). The difference of the calculated heat fluxes on both sides must be equal to the latent heat for given feed and pull rates, i.e., fulfill the Stefan condition [75]. Each point of the melting (M) or crystallization (C) interface is moved by their normal velocity according to the laboratory reference system

$$v_n^{M,C}(t) = \frac{\lambda_S}{\rho_S Q} \frac{\partial T(t)}{\partial n} \Big|_S - \frac{\lambda_L}{\rho_S Q} \frac{\partial T(t)}{\partial n} \Big|_L - V^{M,C}(t) n_z^{M,C}(t) \quad (6.20)$$

where V^M is the feed rate of the poly rod and V^C is the pull rate of the crystal. The indices S and L depict the solid and liquid side of the interface. The shape of the interface is found when the velocity is zero.

p0515 On the open melting front the temperature is also assumed to be $T = T_0$, although the thin liquid film with a thickness around 0.2 mm has a slightly higher temperature [35]. The velocity of the open melting front (O) movement is

$$v_n^O(t) = \frac{\lambda_S}{\rho_S Q} \frac{\partial T(t)}{\partial n} \Big|_S - \frac{q^{rad} - q^{EM}}{\rho_S Q} - V^M(t) n_z^O(t). \quad (6.21)$$

p0520 The shape of the interface is found and the velocity of the open melting front is zero if EM heat sources are balanced by radiation, heat conduction in the poly rod, and latent heat.

26 HANDBOOK OF CRYSTAL GROWTH

p0525 The shape of the free melt surface is calculated as a balance of normal stress considering the surface tension and hydrostatic and EM pressure

$$p_0 - \rho_l g z - \gamma \left(\frac{\cos \phi}{r} + \frac{1}{R'} \right) - p^{EM} = 0 \quad (6.22)$$

where R' is the radius of curvature in the (r,z) plane, ϕ is the angle with the vertical, and p_0 is the reference gauge pressure. For fixed ETP and ITP positions and a given p_0 , the shape of the free surface can be determined minimizing the imbalance of Eqn (22). The value of p_0 is unknown and can be chosen in order to satisfy the Si growth angle and keep the diameter of the crystal constant. Special attention should be paid to the modeling of ETP and ITP where conditions for all encountering interfaces must be satisfied [35].

s0175 6.3.3.6 *Thermomechanical Stress*

p0530 The relation between stress and strain tensors (Hooke's law) in isotropic case for small linear displacements is

$$\sigma_{ij} = \frac{E}{1+\nu} \left(\varepsilon_{ij} + \frac{\nu}{1-2\nu} \varepsilon_{kk} \delta_{ij} \right) - \frac{E\alpha t}{1-2\nu} \delta_{ij} \quad (6.23)$$

where for Si the Young modulus $E = 1.56 \times 10^{11}$ N/m², Poisson's ratio $\nu = 0.25$, and coefficient of thermal expansion $\alpha = 3.2 \times 10^{-6}$ 6/K [47]. Considering that the crystal is in equilibrium state

$$\sigma_{j,j} = 0 \quad (6.24)$$

p0535 and strain-displacement relation

$$\varepsilon_{ij} = \frac{1}{2} (u_{i,j} + u_{j,i}) \quad (6.25)$$

the displacements \mathbf{u} can be found solving the Eqn (24) and fixing the displacement at some point as BC. The second invariant of stress tensor, called von Mises stress [12], is often used for the analysis as a scalar measure, which is representative for the generation of dislocations.

s0180 6.3.3.7 *Transient Modeling*

p0540 The transient model described in Ref. [50] is based on the steady state model [48] but does not account for the convective heat transfer in the melt. The movement at any position of the melting (M) or crystallization (C) interface is defined by their normal velocity in the laboratory reference system in Eqn (20) and the movement of the open melting front (O) in Eqn (21). Knowing these velocities, the calculation of the new positions of the interfaces after a time step Δt is a straightforward task. The volumes of molten and crystallized Si during each time step are calculated as sums over all elements considering the volume change due to feed and pull rates and the volume change due to changed interface positions.

p0545 The difference between molten and crystallized volumes is the change of the melt volume ΔV_{melt} . As the starting point (ETP) and endpoint (ITP) of the free surface are

known (their movements and positions are calculated to fulfill the thermal conditions, as in the quasi-steady model), the new shape of the free surface is calculated iteratively so that the difference between the new and old surface shapes is equal to ΔV_{melt} . The result of the changed free surface is a new melt angle at the ETP, which determines the change of the crystal diameter in the next time step.

p0550 The process control based on the PID algorithm is implemented in the FZoneT software to ensure the growth of the crystal with a predefined shape [52]. The inductor current and the feed rate are adjusted according to the deviation between the actual and desired values for the position of the crystal radius and zone height. The process control is described in more detail in Section 6.2 and in Vol. 2b, Section 10.

s0185 6.3.4 Exemplary Results

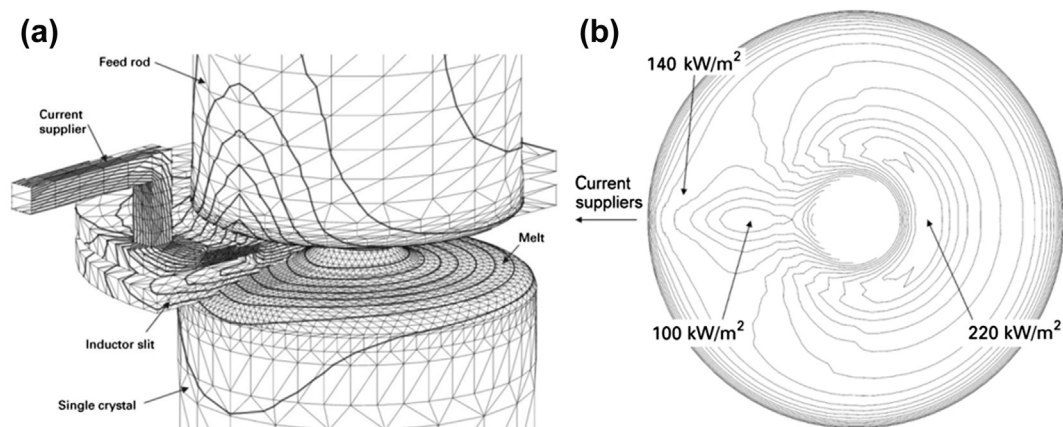
p0555 All results demonstrated in this section are calculated with software included in the program complex FZone [48,49] or in predecessor models [28,34] and are closely related to the work of Prof. Muiżnieks.

s0190 6.3.4.1 *Electromagnetic Field*

p0560 The results of EM field calculations are taken from Ref. [55] and are carried out for the geometry corresponding to the 4" process at the IKZ. All surfaces are assumed axisymmetric, but the inductor is nonsymmetric with its current suppliers having a 1-mm-wide slit between them. The shapes of the open melting front and the free melt surface are taken from the global simulation, i.e., they are calculated using a coupled algorithm also including the 2D calculation of EM pressure and EM heat sources. The surfaces are meshed into triangular boundary elements (Figure 6.15(a)), and the distribution of the surface current density is calculated according to the model described in Section 6.3.3.1. The current on Si surfaces flows almost azimuthally, but in the region of the inductor slit, the current is shifted to the vertical surfaces of feed rod and crystal. The density of EM heat sources on the free surface shows a distinct minimum under the slit at the central part of the free surface (Figure 6.15(b)). The 3D current distribution can be analyzed directly to optimize the inductor shape or used as an input for 3D melt flow simulations. 3D EM field modeling with subsequent azimuthally averaging of heat sources is often used for more precise calculations of 2D interface shapes using the FZone software. The averaging is justifiable due to rotation of crystal and feed rod.

p0565 In spite of the distinct nonsymmetry of the current distribution, 2D modeling of the EM field was a standard procedure in early models [28] and is frequently used during the calculation of interface shapes in order to reduce the computation time nowadays [51,52]. The simple model for the consideration of a narrow inductor slit in 2D reduces the EM field in the central part and increases it in the outer part of Si, making the differences between 2D and 3D even smaller. This effect can be seen in the 2D EM field calculation shown in Figure 6.16, where a part of the field lines goes through the inductor (in a truly 2D case, all lines must go between inductor and the Si surfaces).

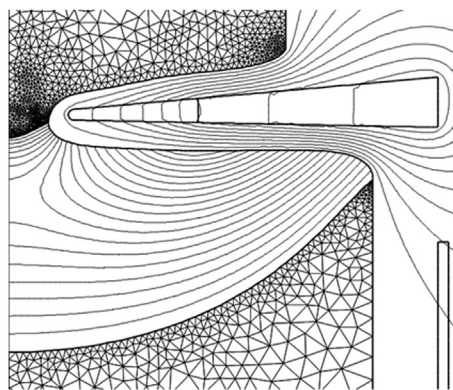
28 HANDBOOK OF CRYSTAL GROWTH



f0080 **FIGURE 6.15** Results of 3D electromagnetic field simulation. View of the model geometry with only half of the inductor shown, triangular boundary elements, and calculated lines of the electric current stream function (a); Joulean power density q_{EM} on the free surface of the melt (b) [55].

s0195 6.3.4.2 Temperature Field

p0570 The calculated temperature field for three different stages of 4" crystal growth with $v_G = 3.3$ mm/min and without a reflector is shown in Figure 6.17 [28]. The interface shapes are a result of the coupled EM and temperature field simulation (the influence of melt flow is not considered here) as described in Section 6.3.3.5. The temperature decreases faster along the vertical axis if the crystal or poly rod is longer due to a larger surface through which the heat can be radiated away. In the case of a short crystal, the crystallization interface has larger deflection and is located closer to the crystal surface to provide larger heat flux to the hotter crystal surface with high radiation.



f0085 **FIGURE 6.16** 2D results showing isolines of magnetic vector potential A, isolines of temperature in the melt with step 2.9 K, and finite element method mesh in poly rod and crystal [35].

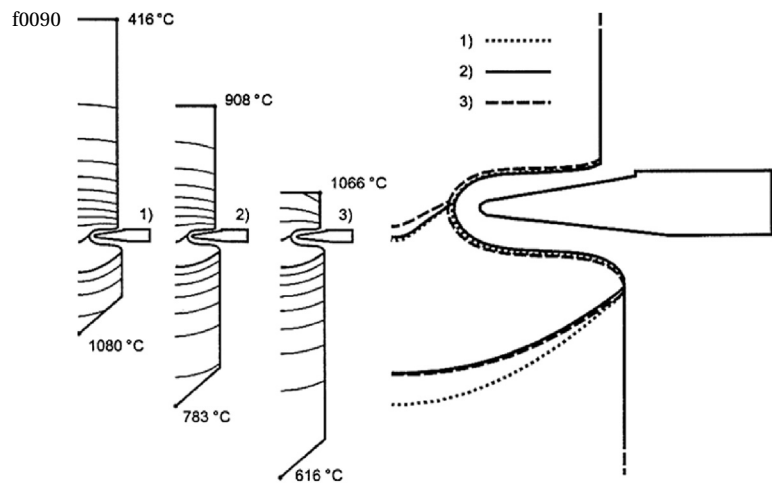


FIGURE 6.17 Temperature field (isolines with step 100 K) and shape of interfaces for three different stages of 4" crystal growth. From Ref. [28].

s0200 6.3.4.3 Melt Flow and Impurity Distribution

p0575 The forces responsible for the melt convection are buoyancy, Marangoni and EM forces. The buoyancy causes downward flow along the cold interfaces and upward flow in the hot region between them. The Marangoni forces cause flow at the free surface toward the interfaces. EM forces at the free surface are directed toward the position of maximum electric current and are opposite to the Marangoni forces.

p0580 The results of transient 2D melt flow in the 4" process for three subsequent time moments with the time step of 2 s are shown in Figure 6.18 [28]. The stream function of meridional flow with two typical vortices (left), the isolines of azimuthal velocity (center), and the isolines of temperature (right) show oscillations, especially near the axis of symmetry. However, the flow is still in laminar regime. Due to the low Prandtl number of 0.013, the temperature field is not strongly influenced by the melt flow—the distribution is similar to one without flow (Figure 6.16).

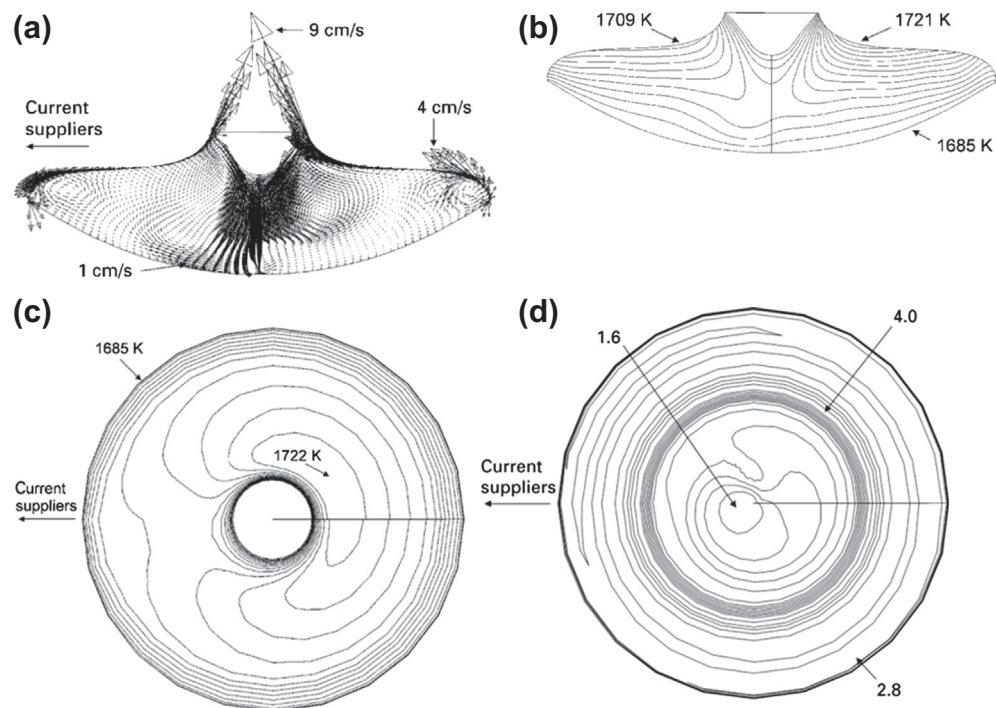
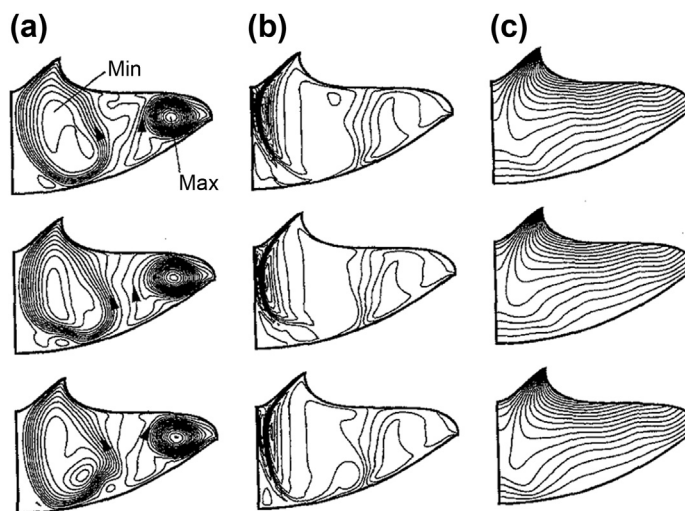
p0585 The meridional convection is reduced when the rotation rate of crystal increases [34]. Nonuniform rotation of crystal causes large vertical gradients of azimuthal velocity at the crystallization interface, which results in meridional forces with a mean value directed toward the center [34].

p0590 The inductor with slits creates a nonsymmetric distribution of Joulean sources and EM forces (Figure 6.16) and, as a result, a 3D melt flow. The results of 3D flow simulation for 4" process is shown in Figure 6.19 [55]. Both velocity (a) and temperature (b, c) distributions show certain nonsymmetry. The resulting dopant distribution at the crystallization interface is nonsymmetric as well (Figure 6.19(d)), and this causes the resistivity striations in a rotating crystal.

p0595 The influence of different types of magnetic fields on the melt flow and RRV in grown crystal is demonstrated using 2D simulation of 4" process corresponding to the

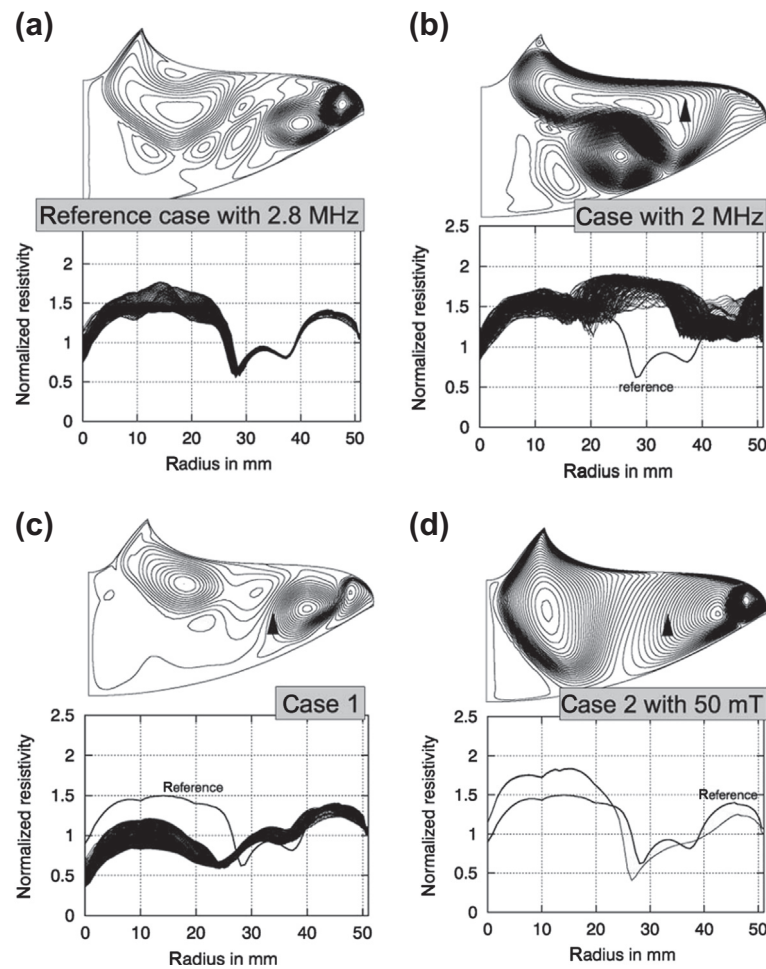
30 HANDBOOK OF CRYSTAL GROWTH

f0095 **FIGURE 6.18** 2D axisymmetric model. Streamlines (a), isolines of azimuthal velocity (b), and isotherms (c) for the three subsequent time moments with the time step of 2 s. From Ref. [28].



f0100 **FIGURE 6.19** Results of 3D melt flow simulation for 4" process. Velocity arrows in vertical cross-section parallel to inductor slit (a), isolines of temperature in the same cross-section (b), isolines of temperature on the free melt surface (c), and dopant concentration at the crystallization interface (d). From Ref. [55].

IKZ facility in Figure 6.20 (from Ref. [41]). For each case, a representative time instant of the stream function of the meridional velocity and several radial resistivity profiles are shown for a time period of 50 s according to an axial length of 2.8 mm in the grown crystal. The mean value of RRV of the standard case (a) is shown in other RRV distributions (b)–(d). The reduction of the frequency of the RF inductor increases the EM forces causing more intense convection and more uniform RRV distribution with increased microscopic fluctuations (Figure 6.20(b)). A magnetic field rotating in the direction of crystal rotation with a frequency of 50 Hz and an intensity of 1 mT also creates slightly more uniform RRV distributions and increased microscopic fluctuations (Figure 6.20(c)). The application of a vertical steady magnetic field of 50 mT



f0105 **FIGURE 6.20** Stream function of meridional velocity and normalized radial resistivity distribution for basic reference case (a), with reduced frequency (b), with rotating magnetic field (c), and with vertical steady magnetic field (d). From Ref. [41].

32 HANDBOOK OF CRYSTAL GROWTH

suppresses the microscopic oscillation of resistivity but makes the RRV less homogeneous (Figure 6.20(d)).

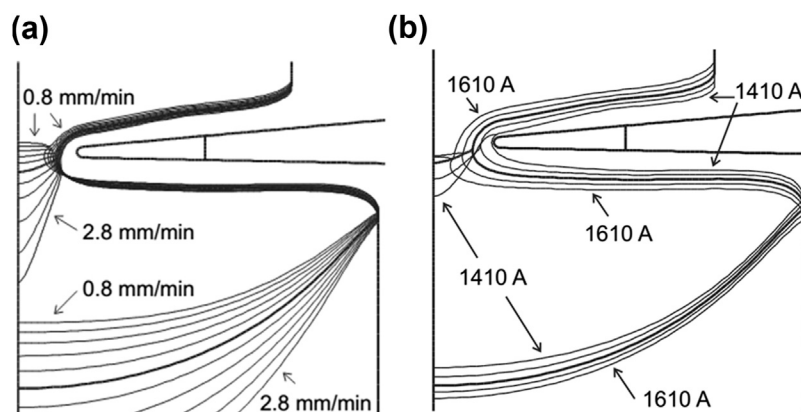
s0205 6.3.4.4 Shape of Interfaces

p0600 The interface shapes are important for the quality of the crystal and crucial for the feasibility of the process, therefore, the dependencies of system geometry and process parameters are of utmost importance. Presented studies are carried out without consideration of melt flow, which was analyzed separately in Section 6.3.4.3.

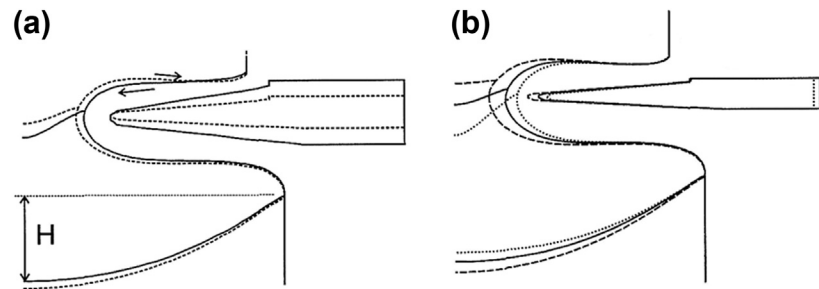
p0605 The effect of the growth rate for an 8" crystal is shown in Figure 6.21(a) for a constant zone height [35]. At higher pull rate, the deflection of the crystallization interface is larger and the open melting front is located closer to the inductor where higher Joulean heat sources are used to compensate the larger latent heat for melting the feed rod with higher feed rate. The deflection of the melting interface gets larger with an increased feed rate and would approach the crystallization interface when further increasing the feed rate.

p0610 The interface shapes at different inductor currents for the 8" system are shown in Figure 6.21(b). The main effect of increasing the inductor current is the increase of zone height and decrease of the neck diameter. The variation of the inductor current for a given inductor geometry is limited by the neck diameter—at large current values the neck is too thin and will break, but for too small current values the neck approaches the inductor surface (it will result in voltage breakdown at a certain distance before touching the inductor).

p0615 The importance of the shape of the inductor is demonstrated in Figure 6.22 for 4" process [34]. If the thickness of the inductor is halved, the process is no longer possible as the part of the melting front has a slope directed outward and the molten Si cannot flow toward the molten zone (Figure 6.22(a)). Increasing the inner diameter of this configuration by 10% assures the melt flow into the molten zone again (Figure 6.22(b)).



f0110 **FIGURE 6.21** Phase boundaries at different crystal pull rates from 0.8 till 2.8 mm/min with a step of 0.2 mm/min (a) and for different inductor currents (zone heights) with 50 Å step (b) for an 8" crystal. From Ref. [35].

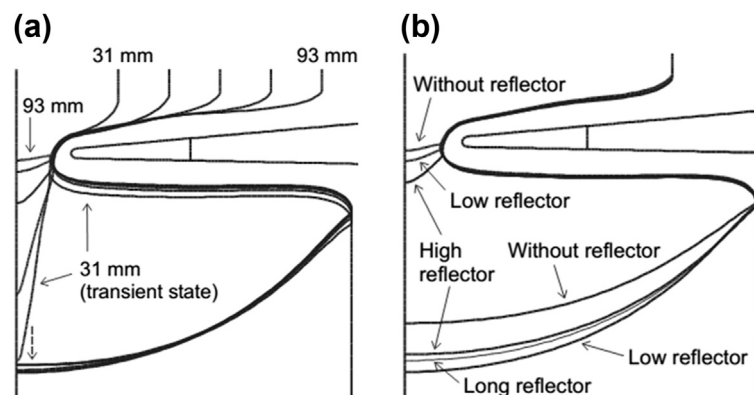


f0115 **FIGURE 6.22** Phase boundaries for various inductor shapes: different heights (a) and different diameters of central hole (b). From Ref. [34].

It can also be seen that the inner diameter of the inductor strongly influences the diameter of the neck and the deflection of the crystallization interface.

p0620 The interface shapes for the 8" process with different diameters of the feed rod are shown in Figure 6.23(a) [35]. The smaller the feed rod diameter, the larger the feed push rate VF and the deeper the deflection of the melting interface. A too small diameter of the feed rod ($r = 31$ mm in Figure 6.23(a)) makes the growth impossible because a solid bridge is built between the polycrystalline feed and the growing monocrystal.

p0625 The effect of the reflector placed around the upper part of the crystal in order to reduce the thermal stress is demonstrated in Figure 6.23(b) [35]. The "low" position of the reflector is shown in Figure 6.16 and in the "high" position the top of the reflector is placed in face of the ETP. In the presence of the reflector, fewer EM heat sources are needed, therefore, the current in the inductor is reduced (from 1600 to 1510 A for reflector in "low" position). Consequently, the maximum temperature difference in the melt is reduced by 13 K and the temperature gradients in melt and crystal are also reduced. As the main part of the heat flux in the crystal is the latent heat, which is not



f0120 **FIGURE 6.23** Phase interfaces for the 8" process with different radii of the feed rod (a) and with different positions of the reflector (b). From Ref. [35].

34 HANDBOOK OF CRYSTAL GROWTH

reduced, the position of the interface at the crystal axis is shifted down toward the region without a reflector to be able to radiate away this amount of heat. Correspondingly, at the “high” position of the reflector, the increase of deflection is not so pronounced.

p0630 The consideration of the effect of the melt flow for 8” crystal results in a smaller deflection of the crystallization interface and a better agreement with the experimental shape [35].

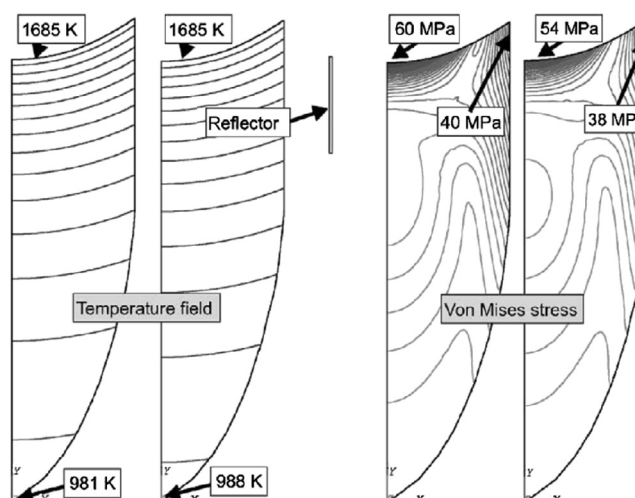
s0210 6.3.4.5 Stress

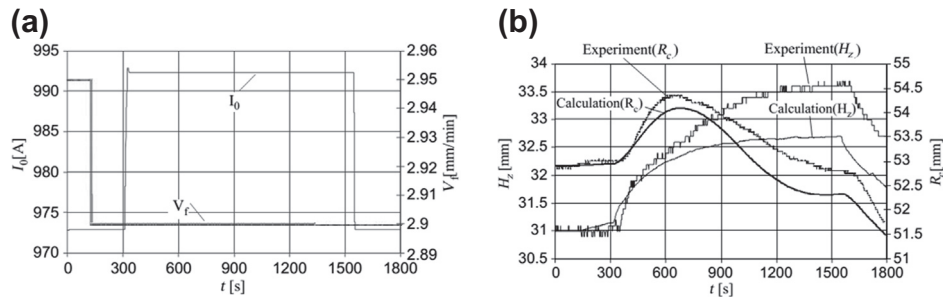
p0635 In Figure 6.24 the results for the 4” crystal with a length of 200 mm corresponding to the IKZ laboratory system are shown with and without reflector [47]. The reflector with a diameter of 140 mm and a height of 40 mm is located 20 mm below the triple point position. The reflector does not deform the temperature field considerably and the minimal temperature at the cone bottom changes slightly. A maximum value of the von Mises stress is on the symmetry axis at the growth interface, and a lower maximum is at the rim of the crystal near the growth interface. The reflector reduces the stress in the center by 6 MPa and at the rim by 2 MPa. It is also shown in Ref. [47] that both maxima increase with increasing the crystal diameter and, especially, when increasing the deflection of the crystallization interface.

s0215 6.3.4.6 Transient Modeling

p0640 The response of the FZ system to the jumps of the inductor current and the feed rod velocity, which are typical process control parameters, are shown as an example of a transient model result and are compared with experiments [51]. The simulation starts from the equilibrium state calculated using the quasi-steady model, and the curves of the inductor current I_0 and the feed rate v_F , as shown in Figure 6.25(a), are applied.

f0125 **FIGURE 6.24** Temperature field with step 50 K and von Mises stress with step 2 MPa for a 4” crystal without (left) and with reflector (right). From Ref. [47].

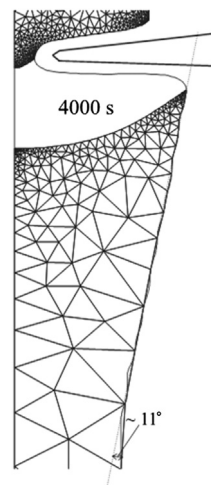




f0130 **FIGURE 6.25** Step-like time dependencies of the feed rod push rate and the inductor current (a) and crystal radius and zone height response (b) during the experiment and calculation [51].

p0645 **Figure 6.25(b)** shows the calculated and measured time dependencies for crystal radius and zone height. Size and location of the calculated crystal radius response are similar to the experimental data. The shapes of the curves agree particularly well. The dependencies of the zone height in calculation and experiment show good agreement, too.

p0650 To ensure the crystal growth with a constant slope, the automatic regulation based on the PID algorithm for I_0 and V_F is implemented in FZoneT. During regulation, I_0 and V_F are adjusted depending on the deviation of the actual and desired values for the slope of the crystal surface and zone height. The constants in the PID algorithm are chosen according to the gathered experiences from calculations with V_F and I_0 jumps. The calculation sample in **Figure 6.26** shows the modeled crystal growth process with a desired slope angle of approximately 11° [52].



f0135 **FIGURE 6.26** A numerically calculated process with automatic regulation for v_F and I_0 that ensures the crystal growth with the given slope angle of 11° , phase boundaries and finite element method mesh 4000 s from the start [52].

s0220 6.3.5 Summary, Conclusions, and Outlook

p0655 Extensive development of coupled multiphysical numerical models during the last 20 years resulted in an effective specialized program packages allowing numerical investigation of numerous aspects of the floating zone process in great detail. The effect of system geometry and process parameters on the shape of interfaces, melt flow, temperature, stress, and dopant distribution is well understood. However, the connection of the calculated macroscopic distributions to dislocation rate and fractures of FZ crystals is still a subject of future investigation. Although the basic effects can be shown using the axisymmetric 2D models, the 3D modeling provides essential improvements of precision mandatory for the simulation-aided process development. The first demonstrations of transient modeling showed a large potential for deeper investigation and optimization of the starting and ending phases of the FZ process as well the use for process control and stability analysis. Many 3D aspects are still not modeled—deviations from the round crystal shape due to ridges, the nonsymmetric and nonuniform melting of the feed rod. The requirements for larger diameters and higher quality crystals will desire challenging technical solutions and then new models have to fulfill those.

References

- [1] Theuerer HC. US Patent No. 3060123; 1952.
- [2] Keck PH, Golay MJE. *Phys Rev* 1953;89:1297.
- [3] Zulehner W. *Mater Sci Eng B* 2000;73:7.
- [4] Lüdge A, Riemann H, Wünscher M, Behr G, Löser W, Muiznieks A, et al. In: Duffar T, editor. *Crystal growth processes based on capillarity*. Wiley-Blackwell; 2010. p. 203.
- [5] Dash WC. *J Appl Phys* 1958;29:705.
- [6] von Ammon W. In: Müller G, Metois JJ, Rudolph P, editors. *Crystal growth – from fundamentals to technology*. Elsevier B.V.; 2004. p. 239.
- [7] Lüdge A, Riemann H. *Inst Phys Conf Ser No 160* 1997:145.
- [8] Lüdge A, Riemann H, Hallmann B, Wawra H, Jensen L, Larsen TL, et al. *High purity silicon VII. Electrochem Soc Proc* 2002;20:75.
- [9] Billig E. *Proc R Soc Lond A* 1955;229:346. Nr. 1178.
- [10] Keller W, et al. German Patent No. DE2626756; 1977.
- [11] Wünscher M. [Thesis]. Berlin: Technische Universität; 2011.
- [12] Menzel R. [Thesis]. Berlin: Technische Universität; 2013.
- [13] von Ammon W, et al. *Electrochem Soc PV* 1993;36:93.
- [14] von Ammon W. US Patent application US 2003/0145781A1.
- [15] Riemann H, Lüdge A. In: Nakajima K, Usami N, editors. *Crystal growth of silicon for solar cells*. Springer; 2009. p. 41.
- [16] Abrosimov N, Luedge A, Muiznieks A, Riemann H. Patent DE 102005016776 A1.
- [17] Paschen F. *Wied Ann Phys* 1889;37:69.
- [18] Ikeda Y, et al. US Patent 4,866,230; 1987.

[AU7]

- [19] Watanabe M, et al. US Patent 4,876,438; 1988.
- [20] Taguchi K, Watanabe M. US Patent 4,931,945; 1988.
- [21] Dornberger E, von Ammon W, Ölkrug H, F. Wasmeier. DE Patent 69601424 T2; 1996.
- [22] Dornberger E, von Ammon W, Ölkrug H, Wasmeier F. US Patent 5,868,831; 1997.
- [23] Werner N. [Thesis]. Berlin: Technische Universität; 2014.
- [24] Ziou D, Tabbone S. Int J Pattern Recognit Image Anal 1998;8:537.
- [25] Becker P, Friedrich H, Fujii K, Giardini W, Mana G, Picard A, et al. Meas Sci Technol 2009;20.
- [26] Becker P, Schiel D. Int J Mass Spectrom 2013;219.
- [27] Borys M, Gläser M, Mecke M. Measurement 2007;40:785.
- [28] Mühlbauer A, Erdmann W, Keller W. J Cryst Growth 1983;64:529.
- [29] Mühlbauer A, Muižnieks A, Virbulis J, Lüdge A, Riemann H. J Cryst Growth 1995;151:66.
- [30] Lie KH, Walker JS, Riahi DN. J Cryst Growth 1990;100:450.
- [31] Lie KH, Walker JS, Riahi DN. J Cryst Growth 1991;109:167.
- [32] Mühlbauer A, Muižnieks A, Jakowitsch A, Virbulis J. Latv J Phys Technol Sci 1992;4.
- [33] Mühlbauer A, Muižnieks A, Jakowitsch A, Virbulis J. Arch für Elektrotechnik 1993;76:161.
- [34] Virbulis J. [Thesis]. Rīga: University of Latvia; 1997.
- [35] Ratnieks G. [Thesis]. Rīga: University of Latvia; 2007.
- [36] Riemann H, Lüdge A, Böttcher K, Rost H-J, Hallmann B, Schröder W, et al. J Electrochem Soc 1995; 142(3):1007.
- [37] Mühlbauer A, Muižnieks A, Virbulis J. J Cryst Growth 1997;180:372.
- [38] Mühlbauer A, Muižnieks A, Raming G, Riemann H, Lüdge A. J Cryst Growth 1999;198/199:107.
- [39] Mühlbauer A, Muižnieks A, Raming G. Cryst Res Technol 1999;34:217.
- [40] Raming G, Muižnieks A, Mühlbauer A. Proc. international colloquium “modelling of material processing”, Rīga; May 1999. 24.
- [41] Raming G, Muižnieks A, Mühlbauer A. J Cryst Growth 2001;230:108.
- [42] Raming G. [Thesis]. Hannover: Institut für Elektrowärme, Universität Hannover; 2000.
- [43] Togawa S, Nishi Y, Kobayashi M. Electrochem Soc Proc 1998;98(13):67.
- [44] Guo Z, Maruyama S, Togawa S. J Cryst Growth 1998;194:321.
- [45] Larsen TL, Jensen L, Lüdge A, Riemann H, Lemke H. J Cryst Growth 2001;230(1–2):300.
- [46] Larsen L. [Thesis]. Technical University of Denmark; 2000.
- [47] Muižnieks A, Raming G, Mühlbauer A, Virbulis J, Hanna B, von Ammon W. J Cryst Growth 2001; 230(1–2):305.
- [48] Ratnieks G, Muižnieks A, Mühlbauer A. J Cryst Growth 2003;255(3–4):227.
- [49] Ratnieks G, Muižnieks A, Mühlbauer A. Proc. international colloquium “modelling of electromagnetic processing” Hanover; March 2003. 205.
- [50] Rudevičs A, Muižnieks A, Ratnieks G, Mühlbauer A, Wetzel Th. J Cryst Growth 2004;266:54.
- [51] Rudevičs A, Muižnieks A, Riemann H, Lüdge A, Ratnieks G, von Ammon W. J Cryst Growth 2005; 275:561.
- [52] Rudevičs A, Muižnieks A, Ratnieks G. Proc. joint 15th Riga and 6th PAMIR conference on fundamental and applied MHD, Riga, vol. 2; June 2005. 229.

38 HANDBOOK OF CRYSTAL GROWTH

- [53] Ratnieks G, Muižnieks A, Raming G, Mühlbauer A, Buligins L. Proc. international colloquium "modelling of material processing" Riga; May 1999. 30.
- [54] Ratnieks G, Muižnieks A, Buligins L, Raming G, Mühlbauer A. *Magneto hydrodynamics* 1999;35(3): 278.
- [55] Ratnieks G, Muižnieks A, Buligins L, Raming G, Mühlbauer A, Lüdge A, et al. *J Cryst Growth* 2000; 216:204.
- [56] Ratnieks G, Muižnieks A, Mühlbauer A, Raming G. *J Cryst Growth* 2001;230:48.
- [57] Lacis K, Muižnieks A, Jekabsons N, Rudevics A, Nacke B. *Magneto hydrodynamics* 2009;45(4):549.
- [58] Lācis K, Muižnieks A, Ratnieks G. *Magneto hydrodynamics* 2005;41(2):147.
- [59] Lācis K, Muižnieks A, Rudevičs A, Sabanskis A. *Magneto hydrodynamics* 2010;46(2):199.
- [60] Muižnieks A, Lācis K, Rudevičs A, Lācis U, Sabanskis A, Plāte M. *Magneto hydrodynamics* 2010;46(4): 475.
- [61] Assaker R. [Thesis]. Belgium: Universite Catholique de Louvain; 1998.
- [62] Bioul F. [Thesis]. Belgium: Universite Catholique de Louvain; 2007.
- [63] Rudevičs A, Muižnieks A, Ratnieks G, Riemann H. *Magneto hydrodynamics* 2005;41(2):123.
- [64] Muižnieks A, Rudevičs A, Lācis K, Riemann H, Lüdge A, Schulze FW, et al. *Magneto hydrodynamics* 2007;43(2):269.
- [65] Menzel R, Rost A, Luedge A, Riemann H. *Cryst Res Technol* 2011;46(10):1003. <http://dx.doi.org/10.1002/crat.201100230>.
- [66] Wünscher M, Menzel R, Riemann H, Lüdge A. *J Cryst Growth* 2014;385:100.
- [67] Barinovs G, Sabanskis A, Muižnieks A. *J Cryst Growth*. <http://dx.doi.org/10.1016/j.jcrysro.2013.12.019>.
- [68] Jackson JD. *Classical electrodynamics*. New York: John Wiley & Sons; 1998.
- [69] Dupret F, Nicodème P, Ryckmans Y, Wouters P, Crochet MJ. *Int J Heat Mass Transf* 1990;33(9):1849.
- [70] Dadzis K, Muižnieks A, Rudevičs A, Ratnieks G. *Magneto hydrodynamics* 2005;41(2):105.
- [71] Rudevics A, Lacis K, Muižnieks A, Jekabsons N, Nacke B. Proc. international scientific colloquium "modelling for electromagnetic processing" Hannover; October 2008.
- [72] Open source library OpenFOAM. <http://www.opencfd.co.uk/openfoam>.
- [73] Muižnieks A, Lacis K, Nacke B. *Magneto hydrodynamics* 2007;43(3):377.
- [74] Surovovs K, Muižnieks A, Sabanskis A, Virbulis J. *J Cryst Growth*. <http://dx.doi.org/10.1016/j.jcrysro.2013.12.066>.
- [75] Stefan J. *Sitzungsber Wiener Akad Math Naturwiss Abt* 1889;98:473.

Abstract:

The floating zone (FZ) technique changed from a crucible-free purification method into a growth technique mainly for high purity silicon crystals. The melt zone is inductively heated by the high frequency magnetic field of a sophisticated one-turn induction coil being the heart of the FZ growth. The needle-eye technique allows for crystals with large diameters beyond the capillary limitations of a cylindrical zone, but both electric breakthrough at the coil slit and bursting of the crystal by thermomechanical stress presently limit the diameter to 200 mm. A novel gFZ concept is depicted that works with granular silicon feedstock instead of expensive feed rods. The automation of the industrial FZ silicon growth is a key issue regarding yield, reproducibility, quality, and economization. A model-based, predictive control system of the FZ growth is presented. For state-of-the-art development and to overcome the process barriers, a detailed multiphysical numerical modeling of the FZ process is required and outlined.

Keywords:

Floating zone technique, Numerical modeling, Process control, Silicon single crystal growth.